Catalysis Communications 186 (2024) 106835

Contents lists available at ScienceDirect

Catalysis Communications

journal homepage: www.elsevier.com/locate/catcom

# $MoO_y$-Pt$(CuNi)_x$ heterojunction nanostructured catalyst for promoting the oxygen reduction reaction activity property

Dezhen Wu [a], Li Qin Zhou [b], Xiaochen Shen [c], Hongfei Jia [b], Zhenmeng Peng [a,c,*]

[a] Department of Chemical, Biomolecular, and Corrosion Engineering, The University of Akron, Akron, OH 44325, United States
[b] Material Research Department, Toyota Research Institute of North America, Ann Arbor, MI 48105, United States
[c] Department of Chemical Engineering, University of South Carolina, Columbia, SC 29208, United States

ARTICLE INFO

*Keywords:*
Oxygen reduction reaction
Catalyst
Pt alloy
Heterojunction structure
Activity property

ABSTRACT

The catalyst intrinsic area-specific activity for the oxygen reduction reaction (ORR) was constrained by the scaling relations governing the adsorption of reaction intermediates. In this study, we strategically modified the electronic band structures of Pt$(CuNi)_x$ alloy nanoparticles by varying their composition, resulting in a specific activity trend resembling a volcano shape. The introduction of $MoO_y$ shattered the existing scaling relations, leading to a significant enhancement in ORR activity of Pt alloys, surpassing the activity of Pt$(CuNi)_x$ catalysts. These findings proved the effectiveness of $MoO_y$ deposition on Pt$(CuNi)_x$ in disrupting the scaling relations, ultimately improving ORR activity.

## 1. Introduction

The demand for clean energy to address the critical climate challenges has attracted intensive research toward the proton exchange membrane fuel cell (PEMFC) technology over the past several decades [1,2]. Because the oxygen reduction reaction (ORR) kinetics is sluggish, roughly two orders of magnitude slower than that of the hydrogen oxidation reaction (HOR), it causes considerable energy loss and thus a major hurdle in the development of PEMFCs [3,4]. The use of a larger amount of platinum catalyst can help to alleviate this challenge, which however raises a significant cost concern. Thus, tremendous efforts have been devoted to the discovery of highly active ORR catalyst materials to decrease the precious metal usage. Previous studies elucidated that alloying Pt with some transition metals can boost the intrinsic ORR activity drastically by tuning the electronic structure (i.e., adjusting the d-band center) of surface Pt active sites [5,6]. Besides, the ORR activity property can also be affected by a few other catalyst particle parameters, like size, morphology, structure and lattice strain [7–11].

In recent years, density function theory (DFT) calculations revealed that the ORR activity can be correlated to the energetics of key reaction intermediates. This leads to a specific activity trend where the ORR activity rises and falls as the adsorption free energies of these reaction intermediates change, namely "volcano plot" [2,12,13]. In detail, ORR is a four-electron transfer reaction in the case of the associative mechanism, involving three major oxygenated reaction intermediates (*O, *OH, and *OOH) [2,14]. However, the adsorption free energies of these three species were found with a strong linear correlation, i.e., following the scaling relation [4,15,16]. Specifically, the binding energies for *O, *OH, and *OOH change monotonically for different metals, which indicates that one variable can be used to describe free energies of all the intermediates due to them being correlated [ 4]. This results in the difficulty to independently tune and optimize the adsorption free energies of these intermediates at the same time because they all change accordingly [2]. Consequently, this scaling relation imposes an upper-limit on the catalyst ORR activity, as a reduction in the energy barrier for one elementary step presumably lead to an increase for another.

To address the activity bottleneck imposed by the scaling relations, extensive exploration has been undertaken to modify the adsorption behavior of intermediates, incorporating strategies such as N, S atom doping [17], introduction of additional adsorption sites [18,19], utilization of strain effects [20], and more [14]. Among these approaches, the incorporation of reducible transition oxides has emerged as a highly effective method for modulating the adsorption energies of reaction intermediates on active sites. In our recent research, the dual-site $SnO_x$/Pt-Cu-Ni heterojunction catalyst demonstrated a remarkable 40% enhancement in the ORR area-specific activity [18]. This enhancement can be attributed to the synergistic interaction between the adjacent Pt

* Corresponding author at: Department of Chemical, Biomolecular, and Corrosion Engineering, The University of Akron, Akron, OH 44325, United States.
*E-mail address:* zmpeng@sc.edu (Z. Peng).

https://doi.org/10.1016/j.catcom.2023.106835
Received 8 November 2023; Received in revised form 22 December 2023; Accepted 26 December 2023
Available online 27 December 2023

site and the metal oxide site, additional adsorption sites by $SnO_x$, the spillover effect with reaction intermediates migrating from the $SnO_x$ site to the adjacent Pt site [18,19,21], and facilitation of oxygen adsorption and bond breakage by tailoring the electronic structure of neighboring Pt sites [19,22]. These synergistic benefits facilitate rapid turnover rates of reaction intermediates, leading to accelerated ORR kinetics, demonstrating a good potential of dual-site catalytic structure for this reaction. However, more heterojunction catalyst systems and comprehensive studies are needed to validate this dual-site ORR catalysis strategy and explore its full potential for improving the reaction kinetics.

In this study, we investigated $MoO_y$-$Pt(CuNi)_x$ heterojunction nanostructures as a new dual-site catalyst system and examined the influences of $MoO_y$ and $Pt(CuNi)_x$ composition on the ORR activity property. A series of octahedral $Pt(CuNi)_x$ alloy nanoparticles were synthesized. With the particle composition controlled by adjusting the stoichiometry between the metal elements, the electronic structure of Pt active sites was fine-tuned within a broad range. The ORR area-specific activity exhibits a volcano-like relationship as a function of the Pt $(CuNi)_x$ composition, with $Pt(CuNi)_{0.66}$ displaying the highest activity of 4.15 mA $cm_{Pt}^{-2}$ at 0.9 V vs. RHE. The $MoO_y$-$Pt(CuNi)_x$ heterojunction nanostructures were obtained by thermal decomposition of $Mo(CO)_6$ on $Pt(CuNi)_x$ followed by air exposure for $MoO_y$ cluster formation. Intriguingly, all $MoO_y$-$Pt(CuNi)_x$ samples exhibit an elevation in the ORR specific activity regardless of the $Pt(CuNi)_x$ composition. Particularly, as high as 5.00 mA $cm_{Pt}^{-2}$ current density is achieved with the $MoO_y$-$Pt(CuNi)_{0.66}$, marking a 14% increase compared to the Pt $(CuNi)_{0.66}$ counterpart. These findings confirm the promoting effect of $MoO_y$ on the $Pt(CuNi)_x$ for catalyzing the ORR and underscore the capability of such heterojunction catalytic structure in disrupting the scaling relation and further improving the ORR activity property.

## 2. Experimental section

### 2.1. Materials

20 wt% Pt on carbon XC-72 (Pt/C) was purchased from Fuel Cell Store. Platinum acetylacetonate ($Pt(acac)_2$, 97%), nickel acetylacetonate ($Ni(acac)_2$, 95%), copper acetylacetonate ($Cu(acac)_2$, 99%), molybdenum hexacarbonyl ($Mo(CO)_6$, ≥99.9%), and chloroform ($CHCl_3$, >99.8%) were purchased from Sigma-Aldrich. Isopropanol ($C_3H_8O$, 99.9%) was purchased from Fisher Scientific. Nafion ionomer solution (5 wt%) was purchased from Ion Power Inc. Perchloric acid ($HClO_4$, 70%) was purchased from ACROS Organics.

### 2.2. Synthesis of $Pt(CuNi)_x$/C alloy nanoparticles

In the standard procedure for synthesizing 20 wt% PtCuNi octahedral alloy nanoparticles on XC-72 carbon (PtCuNi/C), 40 mg (0.1 mmol) of $Pt(acac)_2$, 26.2 mg (0.1 mmol) of $Cu(acac)_2$, and 25.7 mg (0.1 mmol) of $Ni(acac)_2$ were dissolved in 3 mL chloroform. This solution was then drop-wise impregnated onto 80 mg of XC-72 carbon support while continuously stirring. Subsequently, the resulting mixture was promptly transferred to a furnace for the reduction reaction. During the reduction process, the furnace environment was purged with a mixture of $H_2$ at 5 $cm^3$/min and CO at 100 $cm^3$/min. The temperature was incrementally increased from room temperature to 210 °C at a rate of 5 °C/min and maintained at 210 °C for 1 h. Following the reduction, the furnace was purged with argon and allowed to cool down to room temperature. Finally, the synthesized sample was collected for subsequent characterization and testing. All $Pt(CuNi)_x$/C alloys with varied compositions were synthesized using the same procedure, differing only in the quantities of metal precursors employed.

### 2.3. Synthesis of $MoO_y$-$Pt(CuNi)_x$/C heterojunction nanostructures

Following the synthesis of $Pt(CuNi)_x$/C, a solution containing 26.4 mg (0.1 mmol) of $Mo(CO)_6$ in 2 mL of chloroform was meticulously drop-wise impregnated onto the freshly prepared sample. This mixture was swiftly transferred to a furnace, where the system underwent a 20-min purge with argon to establish an inert atmosphere. Subsequently, the temperature was ramped up to 230 °C and maintained for 1 h, facilitating the decomposition of $Mo(CO)_6$. The resulting samples were then collected after the furnace was cooled down to room temperature and denoted as $MoO_y$-$Pt(CuNi)_x$/C. It is known that the decomposition of $Mo(CO)_6$ into metallic Mo can be catalyzed by transition metal that leads to deposition of metallic Mo atoms on the $Pt(CuNi)_x$ surface [26–28], with a rapid oxidation to $MoO_y$ upon exposure to air that forms heterojunction nanostructure of $MoO_y$ on $Pt(CuNi)_x$.

### 2.4. Characterization

X-ray diffraction (XRD) analysis was carried out using a Bruker AXS Dimension D8 X-Ray diffractometer with Cu Ka radiation source. Transmission electron microscopy (TEM) was conducted on a JEOL JEM-1230 microscope operated at 120 KV. High resolution TEM (HRTEM) images, scanning transmission electron microscope (STEM) images, and elemental mappings were taken on a FEI Tecnai G2 F20 microscope operated at 200 KV. Scanning electron microscope (SEM) and energy dispersive X-ray spectroscopy (EDX) were performed on Tescan Lyra 3 XMU equipment at 20.0 KV. X-ray photoelectron spectroscopy (XPS) was executed with VersaProbe II Scanning XPS Microprobe from Physical Electronics (PHI).

### 2.5. Electrochemical measurements

The glassy carbon electrode was polished with alumina powder and thoroughly rinsed with deionized water before any use. In the typical preparation of working electrode, a solution was initially prepared by blending deionized water, isopropanol, and a Nafion ionomer solution (5 wt%) in a volume ratio of 125:100:1. Subsequently, a homogeneous catalyst ink was obtained by finely dispersing 3 mg of the catalyst in 3 mL of the solution and sonicating it for at least 30 mins. Following this, 10 μg of the catalyst ink was drop-casted onto a clean glassy carbon electrode surface, achieving a Pt loading of 10.2 μg/$cm^2_{disk}$.

Electrochemical experiments were performed using a CHI 760D electrochemical workstation (CH Instruments, Inc.) and a rotating disk electrode controller (AFMSRCE, Pine Instrument Co.) in 0.1 M $HClO_4$ electrolyte at room temperature. A Pt wire was used as the counter electrode. A HydroFlex reversible hydrogen electrode (RHE, ET070, Edaq Inc.) was used as the reference electrode to facilitate precise measurements. Prior to testing, either pure $N_2$ (for ECSA evaluation) or $O_2$ (for ORR experiments) gas was bubbled through the electrolyte to attain a saturated electrolyte. To activate the catalyst, cyclic voltammogram (CV) was performed in the potential range of 0.05–1.00 V vs. RHE, employing a scan rate of 100 mV/s for 20 to 40 cycles. The CV curves were recorded in a $N_2$-saturated electrolyte at the scan rate of 50 mV/s. For the ORR polarization curve, measurements were conducted in an $O_2$-saturated electrolyte at a scan rate of 10 mV/s, while the electrode was rotated at 1600 rpm, all conducted at room temperature unless specified otherwise. The kinetic current ($I_k$) was calculated using the Koutecky-Levich equation:

$$\frac{1}{I} = \frac{1}{I_k} + \frac{1}{B\omega^{\frac{1}{2}}} \quad (1)$$

In the Koutecky-Levich equation, I represents the measured current, $I_k$ signifies the kinetic current, x denotes the electrode rotating speed, and B stands for a constant. To compensate for the Ohmic loss resulting from internal resistance, an i-R correction was applied to the ORR activity measurement.

## 3. Results and discussion

Octahedral $Pt(CuNi)_x$/C ternary alloy nanoparticles, where x represents the nominal ratio in the metal precursors (x = 0.33, 0.5, 0.66, 1, 1.5, 2, 3), were synthesized using a modified solid-state chemistry method. They were then characterized and evaluated for their oxygen reduction reaction (ORR) activity [11,23]. The characterization revealed that the $Pt(CuNi)_x$ nanoparticles exhibited a distinct octahedral shape and were evenly distributed on the carbon support, with sizes ranging from 8 to 10 nm, as shown in Fig. S1. Transmission electron microscopy (TEM) imaging showed consistent particle size and morphology across $Pt(CuNi)_x$ samples with varying compositions. The X-ray diffraction (XRD) patterns of these as-prepared samples confirmed the successful formation of face-centered cubic (*fcc*) Pt-Cu-Ni ternary alloy, as was evident from a single set of diffraction peaks with peak position shifts resultant of changes in lattice parameters (Fig. 1). Notably, the characteristic peaks indexed to (111), (200), and (220) planes exhibited shifts toward higher angles as the Ni and Cu contents increased. These shifts indicated lattice shrinkage of $Pt(CuNi)_x$ particles due to the incorporation of Ni and Cu, highlighting the composition-dependent structural changes in the ternary alloy.

Electrochemical measurements were conducted to assess the ORR activity of $Pt(CuNi)_x$ nanoparticle catalysts. Cyclic voltammetry (CV) curves were acquired in a $N_2$-protected 0.1 M $HClO_4$ electrolyte, displaying characteristic signals of hydrogen underpotential deposition and hydroxyl species adsorption in the lower and higher potential ranges, respectively (Fig. S2). Each sample underwent a catalyst activation process, involving repeated CV scans (approximately 20–40 cycles) until the curves stabilized. Subsequently, the electrode was transferred to an $O_2$-saturated 0.1 M $HClO_4$ electrolyte for ORR linear sweep voltammetry (LSV) experiments (Fig. S3). The intrinsic area-specific activity (SA) of the $Pt(CuNi)_x$ catalysts at 0.9 V vs. RHE was calculated by normalizing LSV data with the electrochemically active surface area (ECSA) determined from hydrogen underpotential deposition currents. The dependence of SA on the $Pt(CuNi)_x$ composition was plotted in Fig. 2. Notably, the SA displayed a "volcano" trend concerning the $Pt(CuNi)_x$ composition. The $Pt(CuNi)_{0.66}$ exhibited the highest SA at 4.15 mA/$cm^2_{Pt}$ on average among all examined catalysts, approximately 14 times more active than commercial Pt/C. This enhancement in ORR activity can be attributed to the shift in the d-band center of surface Pt caused by alloying Pt with Cu and Ni, leading to altered adsorption behavior of reaction species and intermediates [24,25]. In this study, the $Pt(CuNi)_x$ composition parameter x was utilized as an indicator of the d-band center as they were correlated, showcasing a monotonous downshift in the d-band center with an increase in x. The optimal $Pt(CuNi)_x$ composition being $Pt(CuNi)_{0.66}$ was identified, achieving balanced adsorption between various reacting species and intermediates, thereby maximizing the ORR activity. The $Pt(CuNi)_{0.66}$ exhibited the highest SA, indicating its optimal composition among all examined $Pt(CuNi)_x$ catalyst materials.

After the evaluation of $Pt(CuNi)_x$ nanoparticle catalysts, $MoO_y$-$Pt(CuNi)_x$ samples were prepared. $Mo(CO)_6$ precursor molecules were deposited on the $Pt(CuNi)_x$ surface, followed by thermal decomposition and oxidation in air, and transformed into $MoO_y$ nanoclusters [26–28]. Fig. 3a shows a representative TEM image of the prepared $MoO_y$-$Pt(CuNi)_{0.66}$/C sample. It indicated an average particle size of 9.9 ± 1.9 nm, which represents a negligible change compared to that of $Pt(CuNi)_{0.66}$ nanoparticles. Notably, the nanoparticles largely retained their octahedral shape after $MoO_y$ deposition. Some minor surface reconstruction was observed in certain particles due to the secondary heat treatment, leading to less defined octahedral shapes, smoother edges and corners. High-resolution TEM (HRTEM) characterizations revealed clear lattice fringes with a measured d-spacing of 0.218 nm (Fig. 3b). This spacing, smaller than that of *fcc* Pt (111), indicated the preservation of the $Pt(CuNi)_x$ alloy structure. Unfortunately, HRTEM imaging was unable to show $MoO_y$, likely due to its low loading (6 at.% in $MoO_y$-$Pt(CuNi)_{0.66}$) and ultrafine cluster size, making it challenging to visualize in the images.

The presence of $MoO_y$ was confirmed through scanning transmission

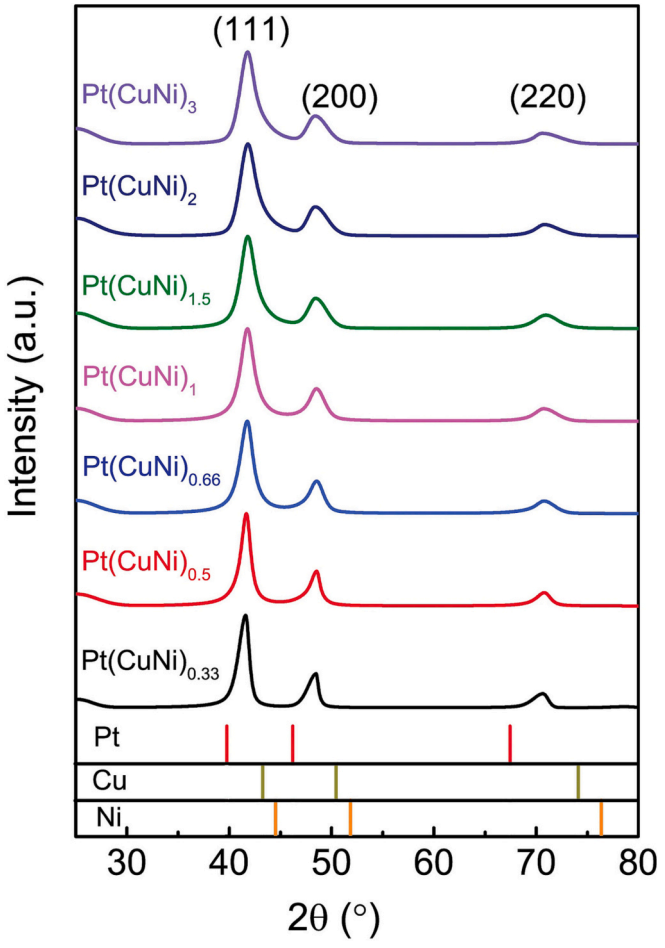


**Fig. 1.** XRD patterns of $Pt(CuNi)_x$/C nanoparticles with varying compositions (x = 0.33, 0.5, 0.66, 1, 1.5, 2, 3). The reference pattern corresponds to pure Pt (JCPDS70–2431).

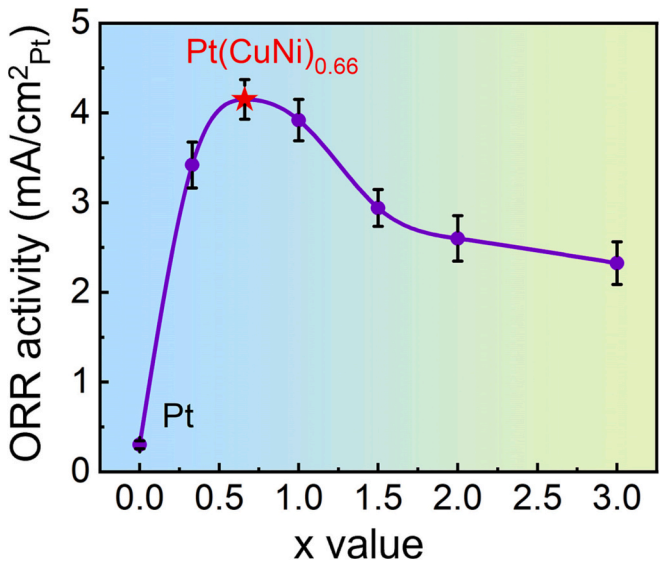


**Fig. 2.** Area-specific activity of $Pt(CuNi)_x$ nanoparticles for the ORR at 0.9 V vs. RHE.

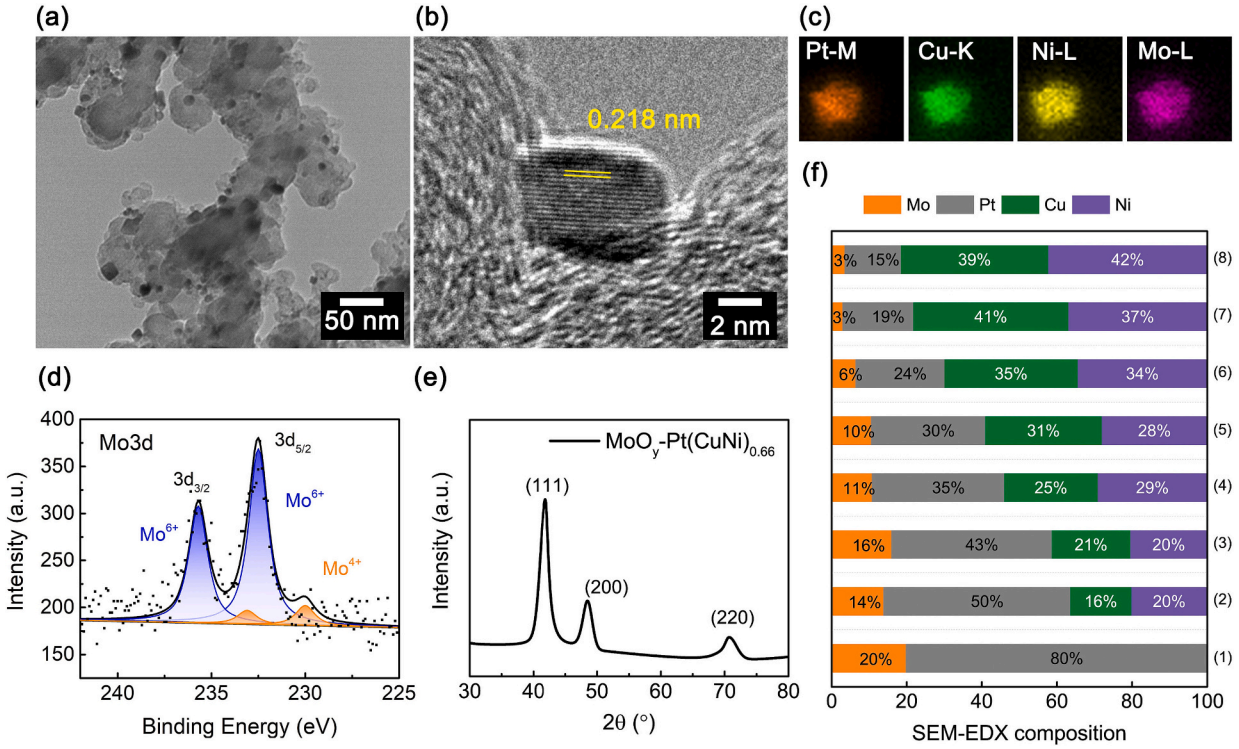


**Fig. 3.** (a) TEM image of $MoO_y$-$Pt(CuNi)_{0.66}$/C, (b, c) HRTEM and STEM images and elemental mapping of an individual $MoO_y$-$Pt(CuNi)_{0.66}$ nanoparticle, (d) Mo 3d XPS spectra and (e) XRD pattern of $MoO_y$-$Pt(CuNi)_{0.66}$/C, (f) EDX determined composition of various $MoO_y$-$Pt(CuNi)_{0.66}$/C samples, with x = 0, 0.33, 0.5, 0.66, 1, 1.5, 2, 3 in (1) ~ (8), respectively.

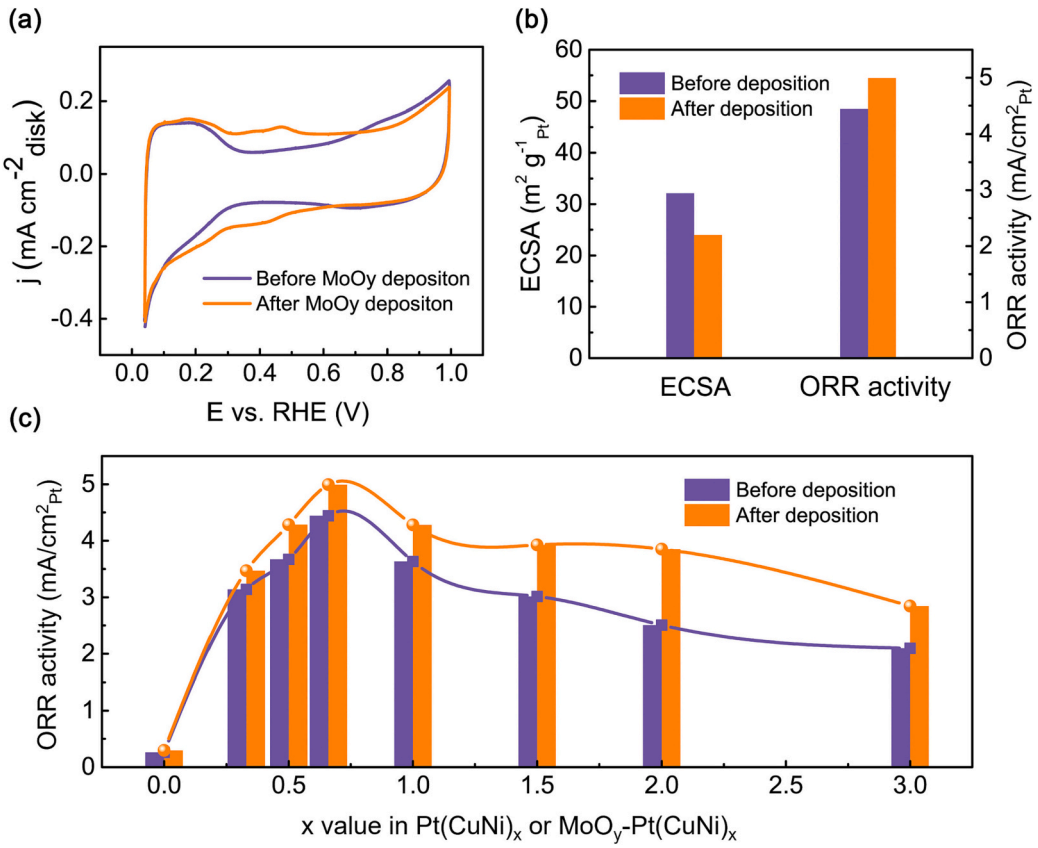


**Fig. 4.** (a) CV curves of $Pt(CuNi)_{0.66}$/C before and after $MoO_y$ deposition in $N_2$-protected 0.1 M $HClO_4$, (b) ECSA and area-specific ORR activity at 0.9 V vs. RHE of $Pt(CuNi)_{0.66}$/C and $MoO_y$-$Pt(CuNi)_{0.66}$/C, (c) Influences of $Pt(CuNi)_x$ alloy composition on the area-specific ORR activity at 0.9 V vs. RHE before and after $MoO_y$ deposition.

electron microscopy-energy dispersive X-ray spectroscopy (STEM-EDS) and elemental mapping of individual $MoO_y$-Pt$(CuNi)_x$ nanoparticles (Fig. 3c and S4). Additionally, X-ray photoelectron spectroscopy (XPS) analysis was conducted to examine the valence state of Mo. The Mo 3d spectrum was deconvoluted into four characteristic spin-orbit peaks (Fig. 3d), corresponding to $Mo^{6+}$ $3d_{3/2}$ at 235.6 eV, $3d_{5/2}$ at 232.5 eV and $Mo^{4+}$ $3d_{3/2}$ at 233.2 eV, $3d_{5/2}$ at 230.0 eV, respectively [29–31]. Quantitative analysis determined the molar ratio of $Mo^{6+}$ to $Mo^{4+}$ to be approximately 7:1 in $MoO_y$. No $Mo^0$ state was detected, ruling out the formation of metallic Mo clusters or the possibility of alloying with Pt $(CuNi)_x$, thus validating the successful deposition of $MoO_y$ on the Pt $(CuNi)_x$ surface. The XRD pattern of $MoO_y$-Pt$(CuNi)_{0.66}$/C exhibited identical peaks to those of Pt$(CuNi)_{0.66}$, indicating that $MoO_y$ deposition had minimal impact on the alloy structure.

SEM-EDS quantitative analysis was employed to characterize the overall composition of $MoO_y$-Pt$(CuNi)_x$ (Fig. 3f). The Pt:Cu:Ni molar ratio in the product was consistent with the feeding ratio of their precursors. Interestingly, the Mo content increased as Pt content increased, which is attributed to Pt's effective catalysis of $Mo(CO)_6$ decomposition [26]. However, we believe that the variation of $MoO_y$ content in different $MoO_y$-Pt$(CuNi)_x$ samples has minimal impact on our fundamental study in this work for the following reasons: (i) The difference in intrinsic ORR activity induced by varying MoOy content was negligible and did not significantly affect the results (Table S1). (ii) The utilization rate of the deposited $MoO_y$ remained uncertain and was anticipated to vary among different alloy nanoparticles due to their distinct compositions. Consequently, the measured Mo content becomes less significant in the context of understanding the underlying working mechanisms. This work focuses on fundamental understanding of the heterojunction nanostructured catalyst, so we believe that the refinement of the synthesis process and precise control of oxide deposition to optimize the ORR activity would be better suited for future research.

The ORR catalytic properties of $MoO_y$-Pt$(CuNi)_x$ were assessed in a 0.1 M $HClO_4$ electrolyte. Fig. 4a presents the CV curves of Pt$(CuNi)_{0.66}$/C before and after $MoO_y$ deposition under $N_2$ atmosphere. The difference between these two curves is due to the redox reactions of $MoO_y$ and a slightly enlarged double-layer capacitance, which validated the effectiveness of the deposition method [32]. Summarized in Fig. 4b, the electrochemically active specific area (ECSA) values, estimated through hydrogen under-potential deposition ($H_{UPD}$), decreased from 32.1 to 24.0 $m^2/g_{Pt}$ after $MoO_y$ deposition. This indicated a total of 25% coverage of the alloy surface by $MoO_y$ deposition. Interestingly, despite the decrease in ECSA, the area-specific ORR activity at 0.9 V substantially increased by nearly 14%, rising from 4.4 to 5.0 mA/ $cm^2_{Pt}$ with the incorporation of $MoO_y$ in Pt$(CuNi)_{0.66}$. Fig. 4c and Fig. S5 summarized the ORR activity property of all examined Pt$(CuNi)_x$/C and $MoO_y$-Pt $(CuNi)_x$/C catalyst samples. It is worth noting that all samples exhibited higher specific activity after $MoO_y$ deposition. Among all, the $MoO_y$-Pt $(CuNi)_{0.66}$ heterojunction nanostructure demonstrated the highest specific activity at 5.0 mA/$cm^2_{Pt}$. The specific activity trend displayed an enlarged volcano-shaped plot concerning x after $MoO_y$ deposition, with Pt$(CuNi)_{0.66}$ remaining to represent the peak with $MoO_y$ clusters on the surface. In our previous study, the dual-site cascade mechanism was extensively investigated [33], indicating that the initial reaction steps could occur on the metal oxide site, followed by the transfer of reaction intermediates to the adjacent Pt site. This SA enhancement provides strong experimental evidence that the activity limit imposed by scaling relations was overcome by $MoO_y$ deposition. Interestingly, the SA enhancement appeared more drastic on Pt-deprived particles (x = 1.0–3.0) than on Pt-rich particles (x = 0–1.0). Previous research has shown that alloying Pt with transition metals shifts the d-band center, and changes in introduced external element content, such as dealloying and leaching, can tune the d-band center of the alloy [34–36]. As a result, Pt-rich nanoparticles inherently have a higher d-band center compared to Pt-deprived nanoparticles. Thus, it suggests that the interaction between Pt and $MoO_y$ has a more significant effect on ORR activity in nanoparticle catalysts with relatively lower d-band centers. Hence, the maximum SA enhancement and the highest overall SA did not coincide due to this interaction's varying impact on nanoparticles with different d-band centers.

Tafel plots for the Pt$(CuNi)_x$ before and after $MoO_y$ deposition were presented in Fig. 5. While determining the exact ORR reaction pathway through Tafel plots is challenging, the Tafel slope offers insights into the characteristics of the rate-determining step [37]. Additionally, changes in the surface coverage of adsorbed reaction intermediates can result in shifts in the measured Tafel slope [38–40]. As illustrated in Fig. 5, for x values ranging from 0 to 1.0, comparable Tafel slopes before and after $MoO_y$ deposition at both high and low potentials did not exhibit a clear trend, suggesting that $MoO_y$ did not significantly alter the reaction kinetics within this composition range. However, for x values from 1.0 to 3.0, the Tafel slope decreased at both high and low potentials after $MoO_y$ deposition for all samples. This reduction indicates faster electron transport, resulting from the decreased coverage of oxygenated intermediates on the Pt surface [37,38,41]. The lowered Tafel slope serves as strong evidence that the reaction kinetics were effectively improved owing to the breaking of scaling relations of intermediates achieved by depositing $MoO_y$. The Arrhenius plots for the ORR kinetic current densities of Pt$(CuNi)_{0.66}$ before and after $MoO_y$ deposition are presented (See Fig. 6). Activation energies for the ORR were calculated at an overpotential of 0.33 V using the Arrhenius equation. Notably, the activation energy for $MoO_y$-Pt$(CuNi)_{0.66}$ was 26.8 kJ/mol, significantly lower than that of Pt$(CuNi)_{0.66}$, which measured at 30.4 kJ/mol. This clear reduction in activation energy underscores the impact of $MoO_y$ deposition, effectively lowering the barrier for ORR. Consequently, this reduction in activation energy has led to a substantial increase in the kinetic current of the ORR, highlighting the efficacy of $MoO_y$ in enhancing the catalytic activity of Pt$(CuNi)_{0.66}$.

## 4. Conclusion

In summary, we successfully synthesized a series of octahedral Pt $(CuNi)_x$/C alloy nanoparticles with varying compositions (x = 0.33, 0.5, 0.66, 1, 1.5, 2, 3). The specific activity of Pt$(CuNi)_x$ for the oxygen reduction reaction (ORR) displayed a volcano trend, with Pt$(CuNi)_{0.66}$ exhibiting the maximum activity. $MoO_y$ was deposited on all freshly synthesized Pt$(CuNi)_x$/C, resulting in $MoO_y$-Pt$(CuNi)_{0.66}$/C dual-site catalysts with a heterojunction nanostructure. The measured ORR specific activities demonstrated up to a 30% increase for all Pt$(CuNi)_x$ compositions after $MoO_y$ deposition. Among the prepared $MoO_y$-Pt $(CuNi)_x$, $MoO_y$-Pt$(CuNi)_{0.66}$ possessed a 25% $MoO_y$ surface coverage of Pt$(CuNi)_{0.66}$ and exhibited the highest specific activity of 5.0 mA/$cm^2_{Pt}$ at 0.9 V vs. RHE. This corresponded to a 14% increase compared to the bare Pt$(CuNi)_{0.66}$ catalyst. Tafel slope studies indicated smaller slopes after $MoO_y$ deposition, signifying faster electron transport resulting from weakened adsorption of oxygenated intermediates to the catalyst surface. Arrhenius plots revealed a smaller activation energy of 26.8 kJ/mol for $MoO_y$-Pt$(CuNi)_{0.66}$ compared to 30.4 kJ/mol for its counterpart Pt$(CuNi)_{0.66}$, indicating enhanced reaction kinetics. This work demonstrates the potential of disrupting the scaling relations of reaction intermediates in ORR through $MoO_y$ deposition to form dual-site heterojunction catalytic structure, offering valuable insights into the design of advanced ORR catalysts.

## Author contributions

D.W. designed and performed the experiments, collected the data, and drafted the manuscript. X.S. contributed to the material synthesis, testing and results discussion. L.Z. provided supervision and conceptualization. Z.P. and H.J. contributed to supervision, conceptualization, reviewing and editing of the manuscript.

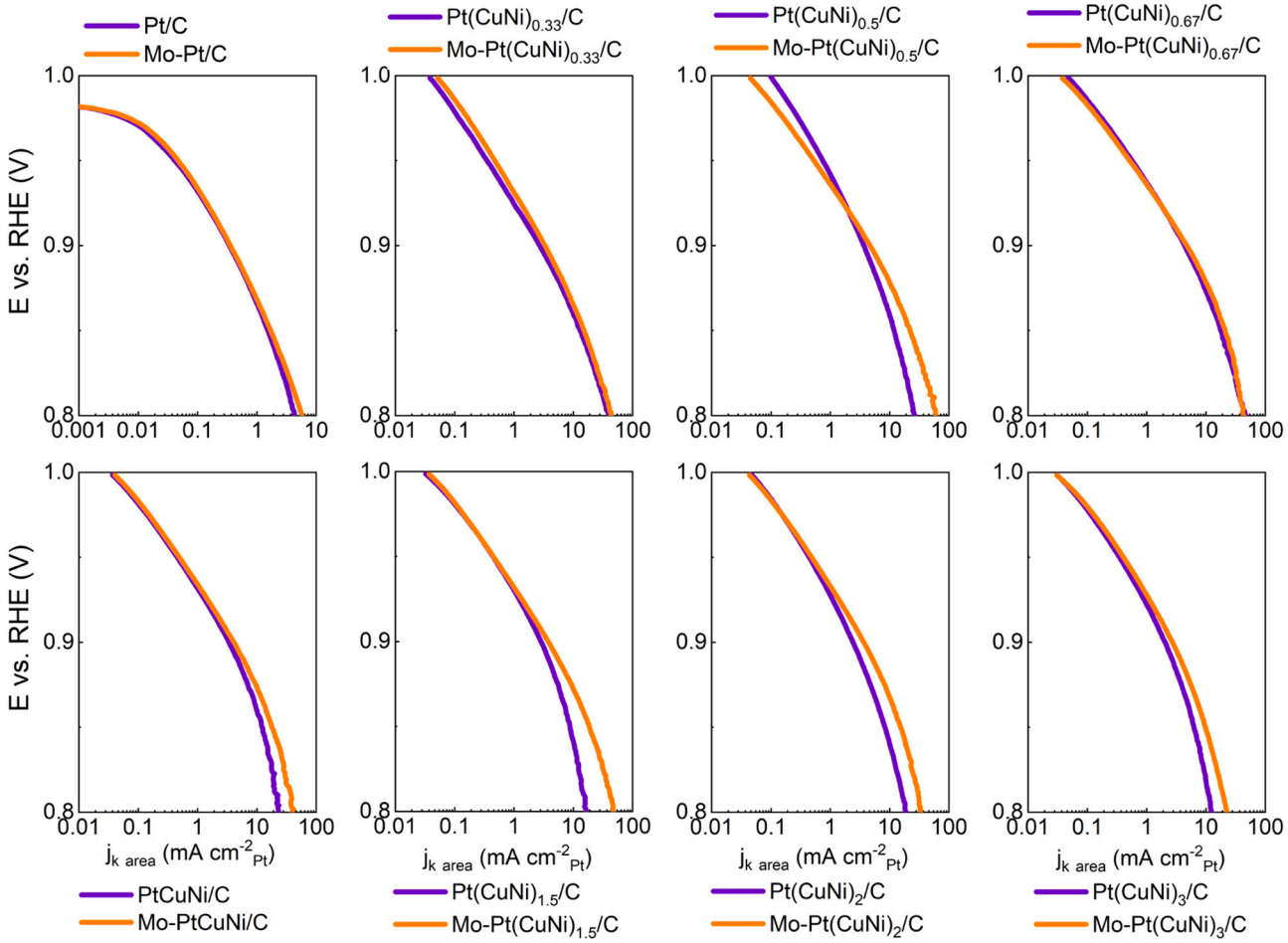


**Fig. 5.** Tafel plots of $Pt(CuNi)_x/C$ and $MoO_y$-$Pt(CuNi)_x/C$ catalysts under ORR testing conditions. X = 0, 0.33, 0.5, 0.67, 1, 1.5, 2, 3 from top left to bottom right, respectively.

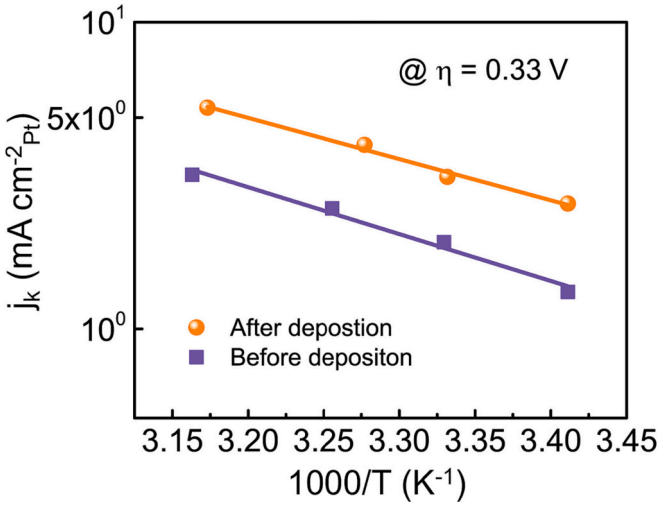


**Fig. 6.** Arrhenius Plots for ORR kinetic current densities at an overpotential of 0.33 V using the $Pt(CuNi)_{0.66}/C$ and $MoO_y$-$Pt(CuNi)_{0.66}/C$ catalysts.

## Notes

Any additional relevant notes should be placed here.

## CRediT authorship contribution statement

**Dezhen Wu:** Conceptualization, Data curation, Formal analysis, Investigation, Methodology, Writing – original draft. **Li Qin Zhou:** Investigation, Writing – review & editing. **Xiaochen Shen:** Investigation, Writing – review & editing. **Hongfei Jia:** Conceptualization, Investigation, Project administration, Supervision, Writing – review & editing. **Zhenmeng Peng:** Conceptualization, Funding acquisition, Project administration, Supervision, Writing – review & editing.

## Declaration of Competing Interest

The authors declare that they have no known competing financial interests or personal relationships that could have appeared to influence the work reported in this paper.

## Data availability

Data will be made available on request.

## Acknowledgment

The authors acknowledge support by National Science Foundation (1955452) and Toyota Motor Corporation. The authors thank Dr. Min

Gao for the technical support with the STEM experiments at Kent State University.

## Appendix A. Supplementary data

TEM images of $Pt(CuNi)_x/C$ alloy nanoparticles; CV and LSV curves of $Pt(CuNi)_x/C$ catalysts in 0.1 M $HClO_4$; STEM-EDS spectra of $MoO_y$-$Pt(CuNi)_{0.66}/C$; LSV curves of $MoO_y$-$Pt(CuNi)_x/C$ catalysts in 0.1 M $HClO_4$; ORR activities of Pt/C, $Pt(CuNi)_x/C$ and $MoO_y$-$Pt(CuNi)_{0.66}/C$. (PDF).

## References


[1] V. Das, S. Padmanaban, K. Venkitusamy, R. Selvamuthukumaran, F. Blaabjerg, P. Siano, Recent advances and challenges of fuel cell based power system architectures and control–a review, Renew. Sust. Energ. Rev. 73 (2017) 10–18.

[2] A. Kulkarni, S. Siahrostami, A. Patel, J.K. Nørskov, Understanding catalytic activity trends in the oxygen reduction reaction, Chem. Rev. 118 (5) (2018) 2302–2312, https://doi.org/10.1021/acs.chemrev.7b00488.

[3] A. Fortunelli, W.A. Goddard, Y. Sha, T.H. Yu, L. Sementa, G. Barcaro, O. Andreussi, Dramatic increase in the oxygen reduction reaction for platinum cathodes from tuning the solvent dielectric constant, Angew. Chem. Int. Ed. 53 (26) (2014) 6669–6672.

[4] J.K. Nørskov, J. Rossmeisl, A. Logadottir, L. Lindqvist, J.R. Kitchin, T. Bligaard, H. Jonsson, Origin of the Overpotential for oxygen reduction at a fuel-cell cathode, J. Phys. Chem. B 108 (46) (2004) 17886–17892.

[5] V.R. Stamenkovic, B. Fowler, B.S. Mun, G. Wang, P.N. Ross, C.A. Lucas, N. M. Markovic, Improved oxygen reduction activity on Pt3Ni(111) via increased surface site availability, Science 315 (5811) (2007) 493–497, https://doi.org/10.1126/science.1135941.

[6] D. Wu, X. Shen, Y. Pan, L. Yao, Z. Peng, Platinum alloy catalysts for oxygen reduction reaction: advances, challenges and perspectives, ChemNanoMat 6 (1) (2020) 32–41.

[7] X.X. Wang, M.T. Swihart, G. Wu, Achievements, challenges and perspectives on cathode catalysts in proton exchange membrane fuel cells for transportation, Nat. Catal. 2 (7) (2019) 578–589, https://doi.org/10.1038/s41929-019-0304-9.

[8] G.-R. Xu, B. Wang, J.-Y. Zhu, F.-Y. Liu, Y. Chen, J.-H. Zeng, J.-X. Jiang, Z.-H. Liu, Y.-W. Tang, J.-M. Lee, Morphological and interfacial control of platinum nanostructures for Electrocatalytic oxygen reduction, ACS Catal. 6 (8) (2016) 5260–5267.

[9] J. Yang, J. Yang, J.Y. Ying, Morphology and lateral strain control of Pt nanoparticles via core–shell construction using alloy AgPd core toward oxygen reduction reaction, ACS Nano 6 (11) (2012) 9373–9382.

[10] D. Wu, X. Shen, L.Q. Zhou, T. Nagai, Y. Pan, L. Yao, B. Zulevi, A. Lubers, H. Jia, Z. Peng, A vacuum impregnation method for synthesizing octahedral Pt2CuNi nanoparticles on mesoporous carbon support and the oxygen reduction reaction electrocatalytic properties, J. Colloid Interface Sci. 564 (2020) 245–253, https://doi.org/10.1016/j.jcis.2019.12.087.

[11] C. Zhang, W. Sandorf, Z. Peng, Octahedral Pt2CuNi uniform alloy nanoparticle catalyst with high activity and promising stability for oxygen reduction reaction, ACS Catal. 5 (4) (2015) 2296–2300, https://doi.org/10.1021/cs502112g.

[12] Y. Zhang, J. Zhang, J. Huang, Potential-dependent volcano plot for oxygen reduction: mathematical origin and implications for catalyst design, J. Phys. Chem. Lett. 10 (22) (2019) 7037–7043.

[13] J. Stacy, Y.N. Regmi, B. Leonard, M. Fan, The recent Progress and future of oxygen reduction reaction catalysis: a review, Renew. Sust. Energ. Rev. 69 (2017) 401–414.

[14] Z.F. Huang, J. Song, S. Dou, X. Li, J. Wang, X. Wang, Strategies to break the scaling relation toward enhanced oxygen Electrocatalysis, Matter 1 (6) (2019) 1494–1518, https://doi.org/10.1016/j.matt.2019.09.011.

[15] Z.W. Seh, J. Kibsgaard, C.F. Dickens, I.B. Chorkendorff, J.K. Nørskov, T. F. Jaramillo, Combining theory and experiment in Electrocatalysis: insights into materials design, Science 355 (6321) (2017) eaad4998.

[16] T.Z.H. Gani, H.J. Kulik, Understanding and breaking scaling relations in single-site catalysis: methane to methanol conversion by FeIV O, ACS Catal. 8 (2) (2018) 975–986.

[17] Y.-Y. Wang, D.-J. Chen, T.C. Allison, Y.J. Tong, Effect of surface-bound sulfide on oxygen reduction reaction on Pt: breaking the scaling relationship and mechanistic insights, J. Chem. Phys. 150 (4) (2019) 41728.

[18] X. Shen, T. Nagai, F. Yang, L.Q. Zhou, Y. Pan, L. Yao, D. Wu, Y.S. Liu, J. Feng, J. Guo, H. Jia, Z. Peng, Dual-site Cascade oxygen reduction mechanism on SnOx/Pt-Cu-Ni for promoting reaction kinetics, J. Am. Chem. Soc. 141 (24) (2019) 9463–9467, https://doi.org/10.1021/jacs.9b02286.

[19] W. Gao, Z. Zhang, M. Dou, F. Wang, Highly dispersed and crystalline Ta2O5 anchored Pt electrocatalyst with improved activity and durability toward oxygen reduction: promotion by atomic-scale Pt-Ta2O5 interactions, ACS Catal. 9 (4) (2019) 3278–3288, https://doi.org/10.1021/acscatal.8b04505.

[20] A. Khorshidi, J. Violet, J. Hashemi, A.A. Peterson, How strain can break the scaling relations of catalysis, Nat. Catal. 1 (4) (2018) 263–268.

[21] Z. Awaludin, J.G.S. Moo, T. Okajima, T. Ohsaka, TaO X-capped Pt nanoparticles as active and durable electrocatalysts for oxygen reduction, J. Mater. Chem. A 1 (46) (2013) 14754–14765.

[22] Y. Lu, Y. Jiang, X. Gao, X. Wang, W. Chen, Strongly coupled Pd Nanotetrahedron/tungsten oxide nanosheet hybrids with enhanced catalytic activity and stability as oxygen reduction electrocatalysts, J. Am. Chem. Soc. 136 (33) (2014) 11687–11697.

[23] C. Zhang, S.Y. Hwang, A. Trout, Z. Peng, Solid-state chemistry-enabled scalable production of octahedral Pt–Ni alloy electrocatalyst for oxygen reduction reaction, J. Am. Chem. Soc. 136 (22) (2014) 7805–7808.

[24] V. Stamenkovic, B.S. Mun, K.J.J. Mayrhofer, P.N. Ross, N.M. Markovic, J. Rossmeisl, J. Greeley, J.K. Nørskov, Changing the activity of electrocatalysts for oxygen reduction by tuning the surface electronic structure, Angew. Chem. Int. Ed. 45 (18) (2006) 2897–2901, https://doi.org/10.1002/anie.200504386.

[25] J. Greeley, I.E.L. Stephens, A.S. Bondarenko, T.P. Johansson, H.A. Hansen, T. F. Jaramillo, J. Rossmeisl, I. Chorkendorff, J.K. Nørskov, Alloys of platinum and early transition metals as oxygen reduction electrocatalysts, Nat. Chem. 1 (7) (2009) 552–556.

[26] I. Usoltsev, R. Eichler, Y. Wang, J. Even, A. Yakushev, H. Haba, M. Asai, H. Brand, A. Di Nitto, C.E. Dullmann, F. Fangli, W. Hartmann, M. Huang, E. Jäger, D. Kaji, J. Kanaya, Y. Kaneya, J. Khuyagbaatar, B. Kindler, J.V. Kratz, J. Krier, Y. Kudou, N. Kurz, B. Lommel, S. Miyashita, K. Morimoto, K. Morita, M. Murakami, Y. Nagame, H. Nitsche, K. Ooe, T.K. Sato, M. Schädel, J. Steiner, P. Steinegger, T. Sumita, M. Takeyama, K. Tanaka, A. Toyoshima, K. Tsukada, A. Türler, Y. Wakabayashi, N. Wiehl, S. Yamaki, Z. Qin, Decomposition studies of group 6 Hexacarbonyl complexes. Part 1: production and decomposition of Mo(CO)6 and W(CO)6, Radiochim. Acta 104 (3) (2016) 141–151, https://doi.org/10.1515/ract-2015-2445.

[27] C.C. Cho, S.L. Bernasek, Molybdenum deposition from the decomposition of molybdenum Hexacarbonyl, J. Appl. Phys. 65 (8) (1989) 3035–3043.

[28] M. Kaltchev, W.T. Tysoe, The decomposition of molybdenum Hexacarbonyl on thin alumina films at high temperatures: formation and reduction of carbides, J. Catal. 196 (1) (2000) 40–45.

[29] J.-G. Choi, L.T. Thompson, XPS study of as-prepared and reduced molybdenum oxides, Appl. Surf. Sci. 93 (2) (1996) 143–149.

[30] P.A. Spevack, N.S. McIntyre, A Raman and XPS investigation of supported molybdenum oxide thin films. 1. Calcination and reduction studies, J. Phys. Chem. 97 (42) (1993) 11020–11030.

[31] G. Kim, Growth and Characterization of Chloronitroaniline Crystals for Optical Parametric Oscillators I, XPS Study of Mo-Based Compounds, 1999.

[32] X. Xiao, C.J. Zhang, S. Lin, L. Huang, Z. Hu, Y. Cheng, T. Li, W. Qiao, D. Long, Y. Huang, Intercalation of cations into partially reduced molybdenum oxide for high-rate Pseudocapacitors, Energy Storage Mater. 1 (2015) 1–8.

[33] X. Shen, T. Nagai, F. Yang, L.Q. Zhou, Y. Pan, L. Yao, D. Wu, Y.S. Liu, J. Feng, J. Guo, H. Jia, Z. Peng, Dual-site cascade oxygen reduction mechanism on SnOx/Pt-Cu-Ni for promoting reaction kinetics, J. Am. Chem. Soc. 141 (24) (2019) 9463–9467, https://doi.org/10.1021/jacs.9b02286.

[34] F. Ando, T. Tanabe, T. Gunji, S. Kaneko, T. Takeda, T. Ohsaka, F. Matsumoto, Effect of the D-Band center on the oxygen reduction reaction activity of electrochemically dealloyed ordered intermetallic platinum–lead (PtPb) nanoparticles supported on TiO2-deposited cup-stacked carbon nanotubes, ACS Appl. Nano Mater. 1 (6) (2018) 2844–2850.

[35] F.H.B. Lima, J. Zhang, M.H. Shao, K. Sasaki, M.B. Vukmirovic, A.E.A. Ticianelli, R. R. Adzic, Catalytic activity− D-band center correlation for the O2 reduction reaction on platinum in alkaline solutions, J. Phys. Chem. C 111 (1) (2007) 404–410.

[36] E. Toyoda, R. Jinnouchi, T. Hatanaka, Y. Morimoto, K. Mitsuhara, A. Visikovskiy, Y. Kido, The D-band structure of Pt nanoclusters correlated with the catalytic activity for an oxygen reduction reaction, J. Phys. Chem. C 115 (43) (2011) 21236–21240.

[37] D.S. Gnanamuthu, J.V. Petrocelli, A generalized expression for the Tafel slope and the kinetics of oxygen reduction on Noble metals and alloys, J. Electrochem. Soc. 114 (10) (1967) 1036, https://doi.org/10.1149/1.2424180.

[38] A. Holewinski, S. Linic, Elementary mechanisms in electrocatalysis: revisiting the ORR Tafel slope, J. Electrochem. Soc. 159 (11) (2012) H864–H870, https://doi.org/10.1149/2.022211jes.

[39] C. Chen, B. Hou, T. Cheng, X. Xin, X. Zhang, Y. Tian, M. Wen, The integration of both advantages of cobalt-incorporated cancrinite-structure nanozeolite and carbon nanotubes for achieving excellent electrochemical oxygen evolution efficiency, Catal. Commun. 180 (2023) 106708.

[40] Y. Yang, J. Yang, P. Liang, Z. Zhang, Z. Li, Z. Hu, V2O3/FeOOH with rich heterogeneous interfaces on Ni foam for efficient oxygen evolution reaction, Catal. Commun. 162 (2022) 106393.

[41] A.E. Russell, Faraday discussions: preface, Faraday Discuss. 140 (2008) 9–10, https://doi.org/10.1039/b814058h.